

X-ray variability of SDSS J000532.84+200717.4: from a normal state to an X-ray weak state

XIAOHUI YANG ¹, YANLI AI ¹, LIMING DOU ², TINGGUI WANG ³, CHICHUAN JIN ^{4,5}, WENFENG WEN,¹
XU ZHANG ¹, YUMING FU ^{6,7}, JINHONG CHEN ⁸, NING JIANG ³, AND FUKUN LIU ^{9,10}

¹Shenzhen Key Laboratory of Ultraintense Laser and Advanced Material Technology, Center for Intense Laser Application Technology, and College of Engineering Physics, Shenzhen Technology University, Shenzhen 518118, People's Republic of China

²Department of Astronomy, School of Physics and Material Sciences, Guangzhou University, Guangzhou 510006, People's Republic of China

³Department of Astronomy, University of Science and Technology of China, Hefei, 230026, People's Republic of China

⁴National Astronomical Observatories, Chinese Academy of Sciences, 20A Datun Road, Beijing 100101, People's Republic of China

⁵School of Astronomy and Space Sciences, University of Chinese Academy of Sciences, 19A Yuquan Road, Beijing 100049, People's Republic of China

⁶Leiden Observatory, Leiden University, Einsteinweg 55, 2333 CC Leiden, The Netherlands

⁷Kapteyn Astronomical Institute, University of Groningen, P.O. Box 800, 9700 AV Groningen, The Netherlands

⁸Department of Physics, University of Hong Kong, Pokfulam Road, Hong Kong, People's Republic of China

⁹Department of Astronomy, School of Physics, Peking University, Beijing 100871, People's Republic of China

¹⁰Kauli Institute for Astronomy and Astrophysics, Peking University, Beijing 100871, People's Republic of China

ABSTRACT

We present a multi-epoch study of the extreme X-ray variability of the type 1 quasar SDSS J000532.84+200717.4 using archival observations from *XMM-Newton*, *Swift*/XRT, *EP-FXT*, and *ROSAT*, together with new optical spectroscopy and multi-wavelength photometry. The 0.2–10 keV X-ray flux exhibits a transition from a high state to a subsequent low state, declining by more than an order of magnitude and placing the source in the X-ray-weak regime ($\Delta\alpha_{\text{ox}} \lesssim -0.3$). Significant variability on timescales of days to weeks persists within the low state. In contrast, the optical and mid-infrared emission remain stable over decade-long timescales, while the UV continuum varies only mildly and broadly tracks the X-ray evolution. Multi-epoch optical spectroscopy shows no significant long-term changes in either the continuum shape or the broad emission-line profiles. The Mg II emission is relatively weak compared with typical quasars, suggesting similarities to weak-line quasars. The pronounced wavelength-dependent variability indicates that the accretion disk remains largely intact while the X-ray emission undergoes dramatic changes. The spectral hardening in the low state and the viability of ionized partial-covering models are consistent with variable, largely dust-free absorbing gas, possibly associated with clumpy inner disk winds, although intrinsic coronal variations cannot be excluded. SDSS J0005+200717.4 therefore provides evidence that extreme X-ray weakness can arise as a transient phase in otherwise normal quasars.

Keywords: Galaxies (573) — Active galactic nuclei (13) — Quasars (1319)

1. INTRODUCTION

The X-ray emission of luminous quasars is widely interpreted as inverse-Compton radiation produced in a hot corona above the accretion disk (Sunyaev, R., & Titarchuk, L. 1980; Yuan, F., & Narayan, R. 2014). The tight empirical relation between the X-ray and ultraviolet (UV) luminosities, commonly parameterized by the

$\alpha_{\text{ox}}-L_{2500 \text{ \AA}}$ correlation, suggests a close coupling between the accretion disk and the X-ray-emitting corona (Tananbaum et al. 1979; Steffen et al. 2006; Lusso & Risaliti 2016; Chira et al. 2026). This relation holds over a wide range of luminosities and provides an important observational constraint on disk-corona physics.

However, a small fraction of type 1 quasars significantly deviate from this standard relation, exhibiting X-ray emission weaker by factors of $\gtrsim 10$ –100 than expected from their UV luminosities. These X-ray-weak quasars challenge the standard picture of disk-corona

coupling and have been the subject of extensive investigation. The prototype of this class, PHL 1811, historically defined the phenomenological properties of X-ray-weak quasars, and is X-ray weak by a factor of ~ 30 – 100 relative to expectations from the $\alpha_{\text{OX}}-L_{2500\text{\AA}}$ relation (Leighly et al. 2007). Thereafter, X-ray-weak AGNs have been reported in both local Seyfert galaxies and high-redshift quasars (i.e., Miniutti et al. (2012), Wu et al. (2012), Luo et al. (2015), Yang et al. (2022), Liu et al. (2022), Jin et al. (2023), Huang et al. (2023)).

Intrinsically X-ray-weak quasars have traditionally been suggested to be rare. Gibson et al. (2008) find that the fraction of X-ray-weak, non-BAL QSO sources underluminous by a factor of 10 comprises $\leq 2\%$ of optically selected SDSS QSOs. A broader investigation by Pu et al. (2020) demonstrates the existence of a population of non-BAL X-ray-weak quasars, reporting that the fractions of quasars in the general population that are X-ray weak by factors of ≥ 6 and ≥ 10 are $5.8\% \pm 0.7\%$ and $2.7\% \pm 0.5\%$, respectively. On the other hand, significantly larger fractions of intrinsic X-ray weakness have been observed in specific extreme quasar subpopulations. For instance, recent work by Nardini et al. (2019) finds a large fraction ($\sim 25\%$) of X-ray-weak quasars in a sample of luminous blue radio-quiet, non-BAL quasars at $z \sim 3$, with no clear evidence of absorption. In addition, Laurenti et al. (2022) report that $\sim 30\%$ of intermediate-redshift, highly accreting ($\lambda_{\text{Edd}} \gtrsim 1$) quasars are intrinsically X-ray weak by factors of ~ 10 – 80 . This result further suggests that extreme accretion conditions, particularly in highly accreting AGNs and NLS1-like systems, may be closely connected to the production of X-ray-weak states.

Two broad classes of physical explanations have been proposed for X-ray-weak quasars. In intrinsic scenarios, the corona is physically weak/inefficient or disk-reflection dominated, leading to suppressed X-ray emission (e.g., Leighly et al. 2007; Miniutti et al. 2012). Alternatively, in absorption-driven models, the central engine remains intrinsically normal, but the observed X-ray emission is attenuated by high-column-density, often ionized gas along the line of sight, such as shielding material associated with disk winds (e.g., Wu et al. 2011; Luo et al. 2015; Ni et al. 2018).

X-ray-weak quasars are frequently associated with weak-line quasars (WLQs), a population characterized by unusually weak high-ionization emission lines (e.g., Fan et al. 1999; Diamond-Stanic et al. 2009; Plotkin et al. 2010b; Cheng et al. 2025; Reich et al. 2026). Previous studies have shown that approximately 30% of X-ray-weak quasars exhibit weak UV emission lines (Wu et al. 2011), while roughly half of WLQs display X-ray weak-

ness (e.g., Luo et al. 2015). This connection suggests that the physical conditions responsible for weak line emission, such as shielding gas or modified ionizing continua, may also play a role in regulating the observed X-ray emission.

Despite such significant progress, distinguishing between intrinsic and absorption-driven scenarios remains observationally challenging, particularly for those objects identified in persistently X-ray-weak states. Multi-wavelength variability provides a critical diagnostic. Almost all of the reported X-ray weak quasars exhibits dramatic X-ray variability with comparatively modest UV and optical changes (e.g., Miniutti et al. 2012; Ni et al. 2020, 2022; Liu et al. 2022; Huang et al. 2026). Strong wavelength dependent variability, especially when accompanied by stable optical emission, indicates that the variability is likely confined to the compact X-ray-emitting region or to material along the line of sight, rather than reflecting a global change in the accretion flow. In this context, quasars that transition between X-ray-normal and X-ray-weak states offer a valuable opportunity to probe the underlying physical mechanisms.

Extreme X-ray variations with amplitude exceeding a factor of 10 or more in AGNs are still rare (e.g., Gibson, R. R., & Brandt, W. 2012; Middei et al. 2017; Timlin et al. 2020; Wang et al. 2025). Strong X-ray variability events have been observed in a few typical type 1 AGNs (e.g. ?; Mehdipour et al. 2021;), which were attributed to changes in the column density of the dust-free obscuring material along the observer’s line of sight. High amplitude changes in X-ray flux were also found in a few cases of changing-look AGNs, associated with significant X-ray spectral variability (e.g., Krumpe et al. 2017; Jana et al. 2021; Grupe et al. 2015; Ai et al. 2020; Liu et al. 2020; Yang et al. 2023). This extreme X-ray variation can be interpreted in the scheme of destruction and re-creation of the inner accretion disc and corona.

Strong and sometimes rapid X-ray variability has been observed in some narrow-line Seyfert 1 galaxies (NLS1s), which are considered to have high or even super-Eddington accretion rates (e.g., Ai et al. 2011; Reeves et al. 2019; Boller et al. 2021; Parker et al. 2021; Jin et al. 2023). Several physical mechanisms have been proposed to explain such extreme X-ray variability in highly accreting AGNs, including intrinsic changes in the X-ray corona, variable absorption by clumpy circumnuclear material, and radiatively driven accretion-disk winds. In particular, rapid changes in coronal geometry or energetics may strongly modulate the X-ray emission while producing only limited optical/UV variability (e.g., Miniutti et al. 2012; Ricci et al. 2020; Wu et al. 2020). At the same time, powerful disk winds

launched via radiation pressure are generally expected in highly accreting systems (e.g., Giustini & Proga 2019; Jiang et al. 2019; Yang, H., & Yuan, F. 2024), and may both intermittently obscure the compact X-ray source and regulate the disk–corona structure.

In this paper, we report the discovery of a dramatic X-ray state transition observed in a radio-quiet quasar SDSS J000532.84+200717.4 ($z = 0.3814$, hereafter SDSS J0005+2007), which undergoes a pronounced transition from an X-ray–normal state to an X-ray–weak phase. SDSS J0005+2007 classified as a Narrow-line Seyfert 1 galaxy in Paliya et al. (2024), and it appears as an unresolved source in optical. By combining multi-epoch X-ray spectroscopy, optical spectroscopy, and long-term multi-wavelength photometric monitoring, we place constraints on the physical origin of the X-ray transition. The X-ray observations and data reduction are presented in Section 2. In Section 3, we analyze the X-ray spectra, variability and present the multi-band variability. We then discuss the physical interpretation of the extreme X-ray variability in Section 4. Finally we provide a summary in Section 5. Throughout this paper, we adopt a flat cosmology with $H_0 = 70 \text{ km s}^{-1} \text{ Mpc}^{-1}$, $\Omega_M = 0.3$, and $\Omega_\Lambda = 0.7$.

2. OBSERVATIONS AND DATA REDUCTION

2.1. X-ray observations and data reduction

SDSS J0005+2007 was serendipitously detected in the field of view of 14 individual *XMM-Newton* observations (Jansen et al. 2001), as shown in Table 1. All observations were taken in full-frame mode, except for those obtained in 2000 and 2006, which were performed in partial-window mode. Data from some individual EPIC cameras were excluded because the source fell near CCD edges or gaps, outside the field of view, or on defective CCD columns.

The European Photon Imaging Camera (EPIC) data were processed using the Science Analysis System (SAS v21.0.0) and the calibration files generated in April 2024. We reduced the EPIC data following the standard procedure described in the SAS Data Analysis Threads. For the EPIC, only single and double events were selected, and bad pixels and high background flares were filtered from the calibrated event lists based on the standard selection criteria. Source spectra were extracted from circular regions with radii ranging from $20''$ to $30''$; background spectra were extracted from source-free regions with a radius of at least 3 times the radius of source regions on the same CCD chip.

We define high- and low-flux states using MOS count-rate threshold of $5 \times 10^{-3} \text{ counts s}^{-1}$ in the 0.2–10 keV band. Observations above this value are classified as

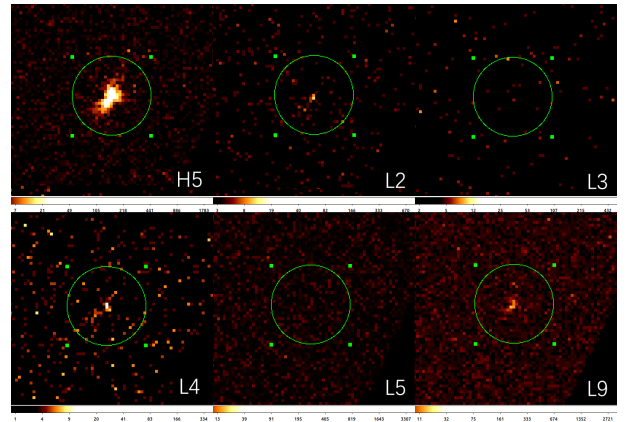


Figure 1. Representative *XMM-Newton* EPIC images of SDSS J0005+2007 at different flux states. The source is clearly detected in the high state (H5), while it becomes weak or undetectable in several low states (L2, L3, L5), demonstrating extreme long-term X-ray variability. The green circle in each image is the circular region of $54''$ with a radius centered on the SDSS position of the source.

high-flux states, while those below it are classified as low-flux states. For the purposes of subsequent analysis, we designate the first five epochs, during which the source was relatively bright, as H1–H5, and the remaining epochs, during which the source was significantly fainter, as L1–L9. Among the nine low-state observations, the source was undetected in L3, L5, L6, and L7. For these epochs, we derived 3σ upper limits on the source count rates using the `uplimit` task within the `ximage` package, adopting a circular extraction region with a radius of $60''$ centered on the optical position of the source. The results are shown in Table 1.

Figure 1 shows representative *XMM-Newton*/EPIC images of SDSS J0005+2007 in the 0.2–10 keV band at different flux states. During the high state (e.g., H5), the source is clearly detected with a compact, high-significance X-ray counterpart. In contrast, during several low-state observations (e.g., L2, L3, and L5), the source is either marginally detected or undetected, with the counts within the extraction region consistent with the background level. Other low-state epochs (e.g., L4 and L9) show weak but significant detections. These images provide a clear view of the dramatic X-ray variability of SDSS J0005+2007.

The *XMM-Newton* X-ray light curve is displayed in Figure 2. The source exhibits pronounced variability over nearly two decades, with count rates decreasing by more than an order of magnitude from the high states observed between 2000 and 2010 to the low states detected after 2015. In particular, the source entered a prolonged X-ray–weak state during 2015–2021, with

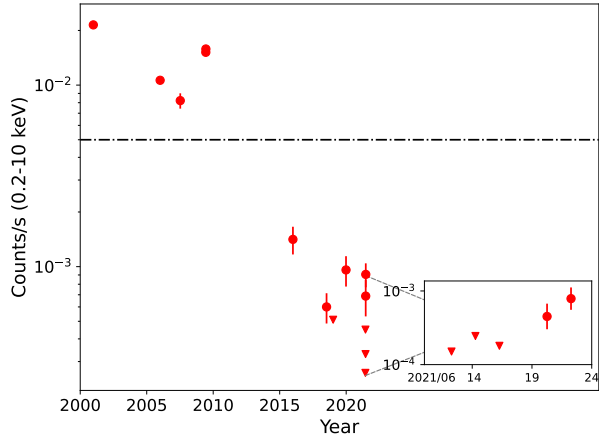


Figure 2. The *XMM-Newton* EPIC-MOS light curve of SDSS J0005+2007 in the 0.2–10 keV band. The horizontal dot-dashed line marks the adopted count-rate threshold of 5×10^{-3} cts s^{-1} , which separates the X-ray high- and low-flux states. The inset shows closely spaced observations in 2021, revealing significant short-term variability with flux changes of a factor of a few on day timescales. Downward arrows indicate 3σ upper limits.

count rates of $\sim (2\text{--}10) \times 10^{-4}$ cts s^{-1} , compared to $\sim 10^{-2}$ cts s^{-1} in earlier epochs. In the sequence of serendipitous *XMM-Newton* observations obtained in 2021 (inset), the source remained X-ray weak but exhibited significant short-term variability, including a gradual brightening by a factor of ~ 3 within ~ 10 days. Several observations yield only upper limits, indicating that the source likely fluctuates around the detection threshold during this low state. Overall, the variability amplitude exceeds a factor of ~ 50 between the historical high and recent low states, demonstrating extreme long-term X-ray variability.

To investigate the long-term X-ray variability of SDSS J0005+2007, we compiled multi-epoch X-ray data from several missions. In addition to the *XMM-Newton* observations, we utilized archival measurements from the Second *Swift* X-ray Telescope Point Source Catalog (2SXPS; Evans et al. 2020) and the *ROSAT* All-Sky Survey Faint Source Catalog (RASS-FSC; Voges et al. 2000). We also include a recent observation obtained with the Einstein Probe Follow-up X-ray Telescope (EP-FXT; Yuan et al. 2022); the data reduction procedure for this observation is described in Section 3.2.

2.2. Optical Spectroscopy

SDSS J0005+2007 was observed by Sloan Digital Sky Survey (SDSS) on 2014 October 7 through a $3''$ diameter fiber over the wavelength range 2600–7500 Å at a spectral resolution of $\simeq 2000$. Follow-up optical spectroscopy

of SDSS J0005+2007 was conducted using the Double Spectrograph (DBSP; Oke & Gunn 1982) mounted on the Hale 200-inch Telescope at Palomar Observatory (P200) on 2024 September 9. The observations were carried out through a $1.5''$ slit using a D55 dichroic, which splits the incoming light between the blue arm (600/4000 grating) and the red arm (316/7500 grating). The grating angles were adjusted to provide a nearly continuous wavelength coverage from ~ 3400 to 10,000 Å (corresponding to $\sim 2500\text{--}7200$ Å in the rest frame). We obtained one more epoch of optical spectroscopy on 2025 December 14 using the Next Generation Palomar Spectrograph (NGPS; Jiang et al. 2018) mounted on the P200 with slit width of $1.5''$. NGPS records simultaneous spectra in two channels, covering approximately 580–780 nm (R channel) and 760–1040 nm (I channel). The data reduction was performed using the *PyPeIt* spectroscopic reduction pipeline (Prochaska et al. 2020), following standard long-slit procedures, including bias subtraction, flat-fielding, and wavelength calibration. The spectrum was extracted using an optimal aperture and flux-calibrated using a standard star observed on the same night.

3. RESULTS

3.1. X-ray spectral Analysis

X-ray spectral fitting was performed using XSPEC v12.13.1 (Arnaud 1996). For the high-flux epochs (H1–H5), the spectra were grouped to a minimum of 10 counts per bin. To improve the signal-to-noise ratio in the faint phase, we constructed a stacked spectrum by combining all low-state observations. Owing to the limited photon statistics, the W-statistic was adopted throughout the analysis. For each epoch, the EPIC pn and/or MOS1/MOS2 spectra were fitted jointly when available.

We first modeled all spectra using a simple power-law modified by Galactic absorption fixed at $N_{\text{H,Gal}} = 1.7 \times 10^{20}$ cm^{-2} (Kalberla et al. 2005). This model provides statistically acceptable fits for most observations. During the high-flux states, the inferred photon indices lie in the range $\Gamma = 2.85\text{--}3.09$, whereas the stacked low-state spectrum yields a photon index of $\Gamma \sim 2.78$, indicating a slightly flatter spectral shape.

We then adopted a composite model consisting of a Galactic-absorbed power law plus a blackbody component (`tbabs*(zpo+zbb)`). For the high-flux states, the addition of the blackbody component leads to a significant improvement in the fit statistics, with typical C-stat ~ 30 compared to the single power-law model. The resulting fits are statistically acceptable, as illustrated

Table 1. X-ray Observation log of SDSS J0005+2007

Obs.ID	Obs.date	Exposure	Instrument	cts s ⁻¹ (10 ⁻³)	Off-axis ^b	Abbr.
	(yyyy-mm-dd)	(ks)		(0.2–10keV)	(arcmin)	
0101040101	2000-12-25	33.8, 33.8	MOS1, MOS2	17.1 ± 0.77, 18.10 ± 0.78	12.7	H1
0306870101	2006-01-03	117.6, 117.6	MOS1, MOS2	12.08 ± 0.34, 10.63 ± 0.32	12.6	H2
0510010701	2007-07-10	15.5, 20.0, 20.1	pn, MOS1, MOS2	3.67 ± 0.18, 7.36 ± 0.69, 6.93 ± 0.67	11.6	H3
0600540601	2009-06-11	114.7, 116.1	MOS1, MOS2	15.31 ± 0.41, 15.16 ± 0.43	11.6	H4
0600540501	2009-06-13	80.9, 80.9	MOS1, MOS2	16.94 ± 0.49, 15.81 ± 0.48	11.6	H5
0741280201	2015-12-30	69.3	MOS2	1.41 ± 0.25	12.6	L1
0780500301	2018-07-11	107.0	MOS2	0.60 ± 0.11	11.6	L2
0831790601	2019-01-08	89.2	MOS2	0.51 ^a	12.6	L3
0854590401	2019-12-27	98.6	MOS2	0.96 ± 0.18	12.5	L4
0842761401	2021-06-14	85.3	MOS2	0.26 ^a	12.6	L5
0842760201	2021-06-16	87.2	MOS2	0.45 ^a	11.8	L6
0842761101	2021-06-18	86.7	MOS2	0.33 ^a	11.7	L7
0842761201	2021-06-20	89.1, 89.7	MOS1, MOS2	0.66 ± 0.17, 0.69 ± 0.16	11.7	L8
0842761301	2021-06-22	88.3, 88.4	MOS1, MOS2	1.10 ± 0.15, 0.91 ± 0.14	11.7	L9

^a The 3 σ upper limits at the epochs of L3, L5, L6, L7.

^b Only the off-axis values of the MOS2 camera are listed here.

in Figure 3. The best-fit parameters for all epochs are summarized in Table 2.

For the stacked low-flux spectrum, the same composite model also provides an acceptable fit, but with noticeably different best-fit parameters. In particular, the power-law component becomes significantly harder ($\Gamma = 1.45_{-0.37}^{+0.38}$) compared to the high-flux states, while the overall flux is reduced by more than an order of magnitude. The addition of an intrinsic absorption component (e.g., *zphabs*) does not lead to a statistically significant improvement in the fit for either the high- or low-flux spectra.

The apparent flattening of the X-ray spectrum in the low state may be attributed to partial-covering absorption. To explore this possibility, we fitted the stacked low-state spectrum with an ionized partial-covering absorber model, *zxcipcf* (Reeves et al. 2008), while fixing the intrinsic continuum shape (photon index and blackbody temperature) to the high-state (H1) values. This model provides a statistically acceptable fit (C-stat/d.o.f. = 29.30/28). The best-fit parameters imply an absorber column density of $N_{\text{H}} \approx 6.8 \times 10^{22} \text{ cm}^{-2}$, an ionization parameter of $\log(\xi/\text{erg/s/cm}) \approx 2.3$, and a high covering fraction ($f_{\text{cov}} \approx 0.73\text{--}1.0$). However, given the limited photon statistics of the low-state spectrum, these parameters remain poorly constrained.

3.2. X-ray and multi-wavelength Variability

The X-ray emission of SDSS J0005+2007 shows extreme variability over both long and short timescales within the *XMM-Newton* epochs, as shown in Figure 2. To extend the temporal baseline beyond the *XMM-*

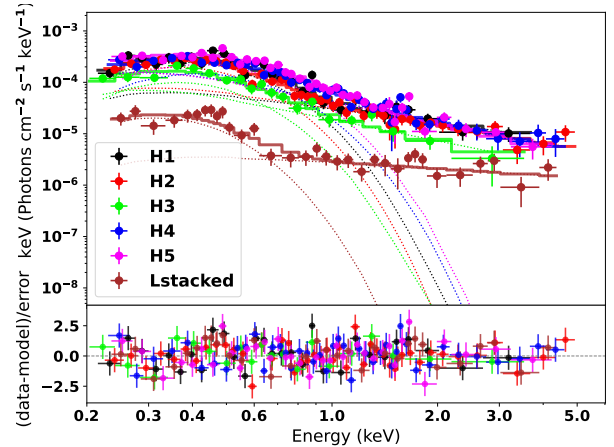


Figure 3. Unfolded *XMM-Newton* EPIC X-ray spectra of SDSS J0005+2007 in different flux states, shown together with the best-fit spectral models consisting of a Galactic-absorbed power law plus a blackbody component. For clarity, only the EPIC-MOS2 data are displayed. The lower panel shows the residuals.

Newton era, we compiled archival X-ray measurements from the ROSAT All-Sky Survey Faint Source Catalog (RASS-FSC) and the *Swift*/XRT 2SXPS catalog. These data provide crucial constraints on the long-term evolution of SDSS J0005+2007 over more than three decades.

SDSS J0005+2007 was detected by ROSAT during the all-sky survey with a count rate of $0.032 \pm 0.013 \text{ cts s}^{-1}$ in a 261 s exposure. The reported ROSAT hardness ratio is $\text{HR} \approx -1$, indicating that the source exhibited a very soft X-ray spectrum at this early epoch. Assuming a Galactic-absorbed power-law model with $\Gamma = 3$, mo-

Table 2. Parameters of X-ray Spectral Fits Using `tbabs*(zpo+zbb)`

Abbr.	T_b	$\log F_b$	Γ	$\log F_p$	$\log F_{\text{soft}}^a$	$\log F_{\text{hard}}^b$	C-stat/d.o.f.
H1	$0.14^{+0.01}_{-0.01}$	$-12.70^{+0.08}_{-0.13}$	$2.24^{+0.36}_{-0.38}$	$-12.88^{+0.07}_{-0.07}$	$-12.38^{+0.03}_{-0.04}$	$-12.73^{+0.04}_{-0.05}$	46.21/29
H2	$0.14^{+0.01}_{-0.01}$	$-12.88^{+0.06}_{-0.09}$	$2.26^{+0.21}_{-0.21}$	$-12.93^{+0.04}_{-0.04}$	$-12.60^{+0.02}_{-0.02}$	$-12.78^{+0.02}_{-0.03}$	55.29/44
H3	$0.13^{+0.01}_{-0.02}$	$-13.03^{+0.12}_{-0.27}$	$2.25^{+0.48}_{-0.54}$	$-13.05^{+0.06}_{-0.07}$	$-12.74^{+0.04}_{-0.04}$	$-12.90^{+0.05}_{-0.05}$	3.66/7
H4	$0.18^{+0.01}_{-0.01}$	$-12.88^{+0.10}_{-0.12}$	$2.54^{+0.16}_{-0.19}$	$-12.63^{+0.03}_{-0.03}$	$-12.38^{+0.02}_{-0.02}$	$-12.54^{+0.02}_{-0.02}$	42.20/43
H5	$0.17^{+0.01}_{-0.01}$	$-12.65^{+0.11}_{-0.16}$	$2.46^{+0.35}_{-0.43}$	$-12.69^{+0.06}_{-0.07}$	$-12.26^{+0.03}_{-0.03}$	$-12.58^{+0.04}_{-0.04}$	45.86/38
Lstacked	$0.11^{+0.02}_{-0.02}$	$-13.82^{+0.09}_{-0.12}$	$1.45^{+0.38}_{-0.37}$	$-14.05^{+0.08}_{-0.10}$	$-13.66^{+0.05}_{-0.07}$	$-13.58^{+0.10}_{-0.10}$	41.28/33

Notes: Columns 2–7 list the blackbody temperature in keV (T_b), blackbody flux in 0.2–2 keV (F_b), photon index (Γ), power-law flux in 0.2–2 keV (F_p), total soft-band flux in 0.2–2 keV (F_{soft}), and hard-band flux in 2–10 keV (F_{hard}), respectively. All fluxes are given in units of $\text{erg s}^{-1} \text{cm}^{-2}$.

tivated by the soft X-ray spectra measured with *XMM-Newton* (Section 3.1), this corresponds to an unabsorbed 0.2–2 keV flux of $4.33 \pm 1.80 \times 10^{-13} \text{ erg cm}^{-2} \text{ s}^{-1}$. This result demonstrates that SDSS J0005+2007 was X-ray bright and spectrally soft at ROSAT epoch.

There are multiple epochs of X-ray detections of SDSS J0005+2007 in the *Swift*/XRT 2SXPS catalog. The *Swift*/XRT count rates were converted to unabsorbed fluxes assuming the same Galactic-absorbed power-law model with $\Gamma = 3$. As shown in Figure 4(a), the *Swift* fluxes are consistent with the historical high-flux level observed during 2000–2010, prior to the transition into the prolonged X-ray-weak state after 2015.

A recent ToO observation with the Einstein Probe Follow-up X-ray Telescope (EP-FXT) provides an independent constraint on the current X-ray state of SDSS J0005+2007. The source was not detected in the EP-FXT observation obtained on 2025 September 15. The resulting 3σ upper limit on the count rate is $1.67 \times 10^{-4} \text{ cts s}^{-1}$ in the 0.5–10 keV band. Assuming the same Galactic-absorbed power-law model ($\Gamma = 3$), this corresponds to a conservative unabsorbed flux upper limit of $\lesssim 1 \times 10^{-14} \text{ erg cm}^{-2} \text{ s}^{-1}$. This non-detection confirms that SDSS J0005+2007 remains in a deep X-ray low-flux state at the most recent epoch (Figure 4(a)).

To investigate the rest-frame ultraviolet behavior of SDSS J0005+2007, we utilized photometric data from the Ultraviolet/Optical Telescope (UVOT; Roming et al. 2005) onboard the *Swift* observatory. The observations were primarily obtained with the UVW2 filter ($\lambda_{\text{eff}} = 1928 \text{ \AA}$), which probes the UV emission near rest-frame 1400 \AA for this quasar. We retrieved the level-2 image files from the HEASoft archive and performed aperture photometry using the `uvotsource` task. Source counts were extracted from a circular region with a radius of $7''$ centered on the optical position of the quasar. This aperture, slightly larger than the standard $5''$ radius, was adopted to account for the extended point-

spread function and to ensure full flux enclosure. The background was estimated from a concentric, source-free annular region. The measured magnitudes were corrected for Galactic extinction using the the extinction law from Schlafly & Finkbeiner (2011).

We show the UVW2 light curve in Figure 4b. It is clear that the UV emission of SDSS J0005+2007 shows a mild long-term fading trend that broadly follows the evolution of the X-ray emission, but with a substantially smaller amplitude of ~ 0.3 mag. In contrast to the dramatic X-ray decline, no sharp UV drop is observed. Instead, the UV flux varies gradually, with epochs of strong X-ray suppression or non-detection generally corresponding to relatively fainter UV levels.

To investigate the optical/mid-infrared variability of SDSS J0005+2007, we compiled archival optical and mid-infrared photometry from Catalina Real-Time Transient Survey (CRTS; Drake et al. 2013), Zwicky Transient Facility (ZTF; Masci et al. 2019), Panoramic Survey Telescope and Rapid Response System (Pan-STARRS; Flewelling et al. 2020), *Gaia* (Gaia Collaboration et al. 2022), and Near-Earth Object Wide-field Infrared Survey Explorer Reactivation Mission (*NEOWISE*; Mainzer et al. 2011; WISE Team 2020). We used the forced photometry from ZTF and Pan-STARRS. As shown in Figure 4, the optical and mid-infrared light curves do not exhibit any substantial long-term variability, remaining stable over timescales of years to decades. The observed variability amplitudes are much smaller than those seen in X-rays, indicating a clear decoupling between the extreme X-ray variability and the emission at longer wavelengths.

3.3. Optical Spectroscopy

Figure 5 presents the rest-frame optical spectra of SDSS J0005+2007 obtained at three different epochs. All spectra have been corrected for Galactic extinction and shifted to the rest frame assuming a redshift of $z = 0.3814$. The P200/DBSP and P200/NGPS spec-

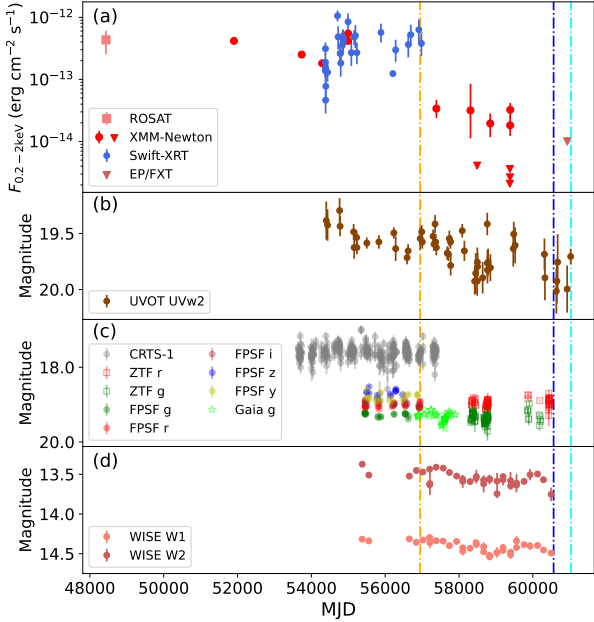


Figure 4. Multi-wavelength light curves between 1991–2025 of SDSS J0005+2007. (a) X-ray light curve in the 0.2–2 keV band compiled from *XMM-Newton*, ROSAT, *Swift*/XRT, and EP-FXT observations. For epochs with non-detections, 3σ upper limits are shown. The vertical dot-dashed lines mark the epochs of the SDSS and P200 spectroscopic observations. (b) Ultraviolet light curve from *Swift*/UVOT in the UVW2 band. (c) Optical light curves from CRTS, ZTF, Pan-STARRS, and *Gaia*. (d) Mid-infrared light curves from the *WISE*/NEOWISE W1 and W2 bands, which were binned into 7-day intervals with the mean magnitude shown.

tra were flux-recalibrated by scaling their narrow [O III] $\lambda 5007$ emission-line fluxes to match that of the SDSS spectrum. The optical spectra of SDSS J0005+2007 remain remarkably stable over timescales of years to decades. Despite the extreme variability observed in the X-ray band, the broad emission lines have remained remarkably stable over the past decade. This behavior suggests that the photoionizing continuum incident on the broad-line region has not undergone significant long-term changes or been obscured.

We modeled the SDSS optical spectrum using the PyQSOFit code (Guo et al. 2018) and performed spectral decomposition to derive the key physical parameters of the source. After subtracting the host-galaxy contribution, we measured an AGN continuum flux density at 5100 \AA of $F_{5100} = 7.07 \times 10^{-17} \text{ erg s}^{-1} \text{ cm}^{-2} \text{ \AA}^{-1}$ and a full width at half maximum (FWHM) of the broad $H\beta$ component of $1823.32 \text{ km s}^{-1}$. These values are consistent with those reported by Rakshit et al. (2020), who also classified the source as an NLS1 galaxy. Using the continuum luminosity at 5100 \AA

(L_{5100}) and the FWHM of the broad $H\beta$ emission line, we estimated the single-epoch (SE) virial black hole mass following the calibration of Shen et al. (2024), obtaining $M_{\text{BH}} \approx 3.18 \times 10^7 M_{\odot}$ from the SDSS spectrum. Applying the bolometric correction of Dalla Bontà et al. (2020), we derived a bolometric luminosity of $L_{\text{bol}} \approx 2.56 \times 10^{45} \text{ erg s}^{-1}$ and an Eddington ratio of $\lambda_{\text{Edd}} \approx 0.614$. We further estimated the black hole mass using the empirical relation based on the broad $H\alpha$ luminosity and the FWHM of the broad $H\alpha$ emission line (Greene & Ho 2005), obtaining $M_{\text{BH}} \approx 1.06 \times 10^7 M_{\odot}$.

As discussed by Dalla Bontà et al. (2020), SE virial black hole masses based on broad $H\beta$ may be systematically overestimated in highly accreting AGNs. We therefore additionally applied Equation (30) of Dalla Bontà et al. (2020), which accounts for the Eddington-ratio dependence, obtaining an alternative estimate of $M_{\text{BH}} \approx 2.66 \times 10^6 M_{\odot}$. The Eddington-ratio-corrected black hole mass is approximately one order of magnitude lower than the standard SE virial estimate, implying that SDSS J0005+2007 may be accreting at an even higher Eddington ratio than inferred from the uncorrected mass estimate.

From the same spectral fits, we measured the rest-frame equivalent widths (REWs) of the Mg II emission line, finding $\text{REW}_{\text{Mg II}} \approx 9.68 \text{ \AA}$ from the SDSS spectrum and $\approx 24.32 \text{ \AA}$ from the P200 spectrum. These values are lower than the typical range for quasars ($\sim 30\text{--}50 \text{ \AA}$) and fall within the regime commonly associated with WLQs (e.g., Diamond-Stanic et al. 2009; Plotkin et al. 2010b). However, a definitive WLQ classification generally requires constraints on high-ionization lines, most notably $\text{REW}_{\text{C IV}} \lesssim 10 \text{ \AA}$. In the absence of rest-frame UV spectroscopy, we cannot conclusively determine whether SDSS J0005+2007 belongs to the WLQ population. Nevertheless, the relatively weak Mg II emission suggests potential physical similarities, such as the possible presence of shielding gas that modifies the ionizing continuum incident on the broad-line region.

Given the possible WLQ-like nature of SDSS J0005+2007 together with its high-accretion NLS1 properties, previous studies have suggested that Fe II-corrected virial black hole mass estimates may be more appropriate for such systems (e.g., Du & Wang 2019; Ha et al. 2023). From the spectral decomposition, we measured an integrated optical Fe II flux of $F_{\text{Fe}} \approx 584.02 \times 10^{-17} \text{ erg s}^{-1} \text{ cm}^{-2}$ over the $4434\text{--}4684 \text{ \AA}$ rest-frame range and a broad $H\beta$ flux of $F_{\text{H}\beta}^{\text{br}} \approx 367.24 \times 10^{-17} \text{ erg s}^{-1} \text{ cm}^{-2}$, yielding a strong optical Fe II emission strength of $R_{\text{Fe II}} = F_{\text{Fe}}/F_{\text{H}\beta}^{\text{br}} \approx 1.59$. Applying the prescription of Du & Wang (2019), we derived an Fe II-corrected black hole mass of

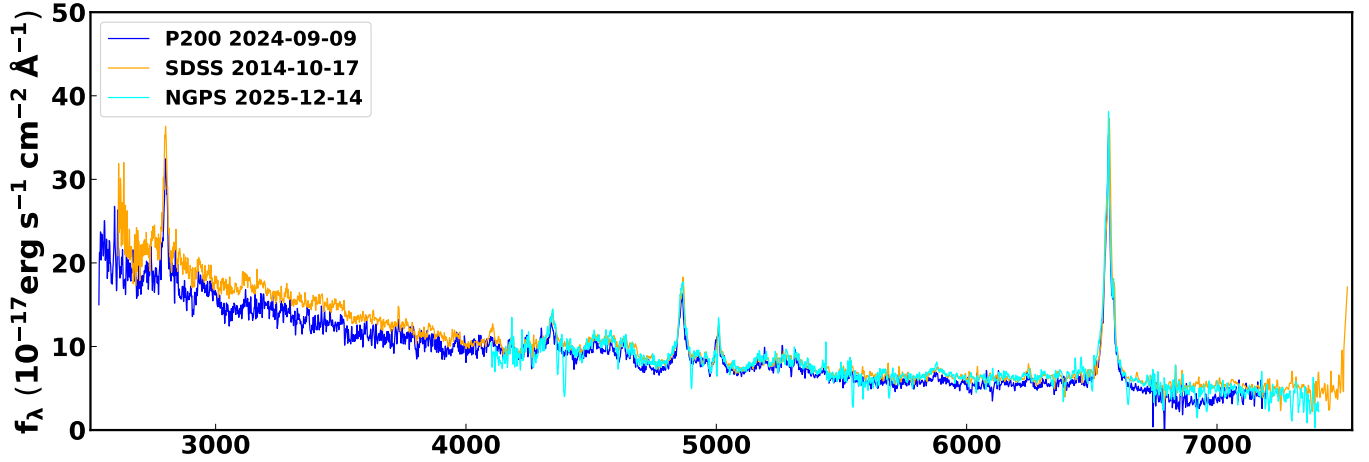


Figure 5. Rest-frame optical spectra of SDSS J0005+2007 obtained at three epochs: 2014 October 17 from SDSS (orange line), 2024 September 09 from P200/DBSP (blue line), and 2025 December 14 from P200/NGPS (cyan line). All spectra have been corrected for Galactic extinction and shifted to the rest frame with $z = 0.3814$. The fluxes of the P200 and NGPS spectra were recalibrated by scaling their narrow [O III] $\lambda 5007$ emission line flux to match that of the SDSS spectrum.

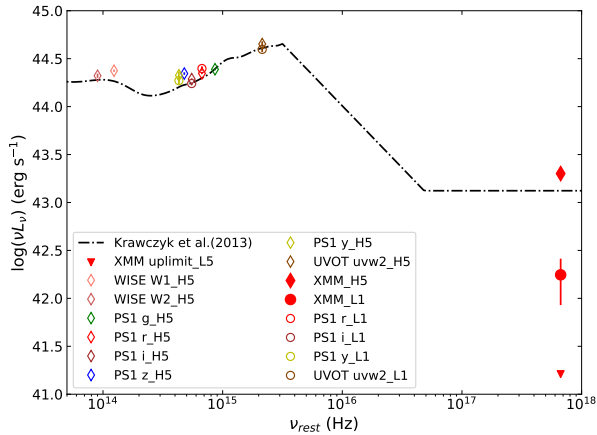


Figure 6. Infrared-to-X-ray spectral energy distributions (SEDs) of SDSS J0005+2007 in the X-ray high state and low state. The IR-to-UV data points represent quasi-simultaneous observations during the X-ray high state (H5; diamonds) and the low state (L1; circles). The red downward triangle denotes the 3σ upper limit from the undetected X-ray epoch (L5). For comparison, the black dot-dashed line shows the mean SED of radio-quiet quasars from Krawczyk et al. (2013), normalized to the 5100 \AA flux of SDSS J0005+2007.

$M_{\text{BH}} \approx 1.50 \times 10^7 M_{\odot}$, broadly consistent with the standard $H\beta$ -based virial mass estimate.

3.4. Spectra Energy Distribution

Figure 6 presents the rest-frame broadband SED of SDSS J0005+2007, combining multi-wavelength photometry from the infrared to the X-ray bands. We compare the data obtained during the X-ray high state (H5)

and the low state (L1/L5) with the standard radio-quiet quasar template of Krawczyk et al. (2013). In the high state (H5), the source emission (diamonds) closely follows the standard template across the infrared, optical, UV, and X-ray bands, with the X-ray luminosity consistent with that expected for a typical type 1 quasar.

In contrast, the low state reveals a clear decoupling between the optical-UV and X-ray emission components. In the infrared and optical bands, the low-state data points (circles) remain comparable to those in the high state, showing only modest scatter without a systematic flux decrease. The UV emission exhibits a mild decline, but its amplitude remains small compared to the dramatic changes observed in the X-ray regime. The X-ray flux in the low state drops by more than an order of magnitude, and the deepest upper limit at epoch L5 lies nearly two orders of magnitude below the template prediction. This SED evolution indicates that the extreme X-ray weakness occurs while the optical-UV emission remains broadly consistent with that of a luminous accretion disk.

To systematically quantify this behavior, we computed the X-ray-to-optical power-law slope, $\alpha_{\text{ox}} = 0.3838 \log(L_{2 \text{ keV}}/L_{2500 \text{ \AA}})$ (Tananbaum et al. 1979), for five epochs (H3, H5, L1, L4, and L9) with quasi-simultaneous UV and X-ray observations. The rest-frame 2500 \AA luminosities were derived from the UVW2 photometry, assuming a spectral slope of $\alpha_{\lambda} = -1.57$, inferred from the SDSS spectral modeling. During the high states, the inferred α_{ox} values range from -1.33 to -1.53 , consistent with those of typical quasars. In contrast, the low-state measurements (L1, L4, and L9) show significantly steeper slopes of $\alpha_{\text{ox}} \lesssim -1.70$, while

the deepest non-detection at epoch L5 implies an upper limit of $\alpha_{\text{ox}} \approx -2.13$.

To further characterize the X-ray weakness, we computed $\Delta\alpha_{\text{ox}} = \alpha_{\text{ox,obs}} - \alpha_{\text{ox,exp}}$, where $\alpha_{\text{ox,exp}}$ is the expected value from the $\alpha_{\text{ox}}-L_{2500\text{\AA}}$ relation of [Stefen et al. \(2006\)](#). The low-state observations yield $\Delta\alpha_{\text{ox}} \lesssim -0.3$, corresponding to an X-ray weakness factor of $f_{\text{weak}} = 10^{-\Delta\alpha_{\text{ox}}/0.384} \gtrsim 6$, placing the source in the X-ray-weak regime (e.g., [Pu et al. 2020](#)).

4. DISCUSSION

The luminous NLS1 SDSS J0005+2007 presents extreme X-ray variability over timescales of decades, in particular a systematic decline in the soft X-ray flux by a factor of ~ 10 over a timescale of ~ 5 yr. In contrast, the UV emission varies only mildly (~ 0.3 mag), while the optical continuum, broad emission-line profiles, and mid-infrared emission remain remarkably stable over decade-long timescales. During the high states, the X-ray spectrum is persistently soft ($\Gamma \gtrsim 2.5-3$), typical of luminous type 1 quasars, whereas the stacked low-state spectrum shows substantial flux suppression together with indications of spectral hardening. These combined variability and spectral properties provide the observational framework for interpreting the physical origin of the X-ray transition.

4.1. Nature of the X-ray Weakness

A key question raised by the extreme X-ray variability of SDSS J0005+2007 is whether it reflects a global change in the accretion flow. Several observational results argue against this interpretation. The optical and mid-infrared emission remain stable over timescales of years to decades, and multi-epoch optical spectroscopy reveals no significant long-term changes in either the continuum level or the broad emission-line profiles. The persistence of the broad-line region (BLR) properties indicates that the photoionizing continuum incident on the line-emitting gas has not undergone substantial long-term variation. In addition, the UV luminosity exhibits only mild variability compared to the dramatic X-ray evolution. Taken together, these results suggest that the optical-UV emitting accretion disk remains largely intact during the X-ray low states, disfavoring a global shutdown of accretion.

In contrast, the X-ray emission declines by more than an order of magnitude, and by nearly two orders of magnitude in the deepest epoch. Two broad classes of mechanisms may account for such behavior: absorption along the line of sight or intrinsic changes in the X-ray corona.

The spectral hardening observed in the stacked low-state spectrum is qualitatively consistent with obscuration. When the intrinsic continuum shape is fixed

to the high-state values, an ionized partial-covering absorber ($N_{\text{H}} \approx 6.8 \times 10^{22} \text{ cm}^{-2}$, $\log(\xi/\text{erg cm s}^{-1}) \approx 2.3$) provides an acceptable description of the low-state spectrum. Although the photon statistics do not tightly constrain these parameters, this model demonstrates that a moderate column of ionized gas can reproduce both the observed flux suppression and the spectral shape. Such a scenario is broadly consistent with the interpretation proposed for other X-ray-weak quasars. For example, PHL 1811 analogs and weak-line quasars are often associated with shielding gas that attenuates the ionizing continuum (([Wu et al. 2011](#); [Luo et al. 2015](#); [Ni et al. 2018, 2022](#))). The presence of disk winds, inferred from weak, blueshifted, and asymmetric C IV emission lines, and the hard X-ray spectral properties revealed by stacking analyses further support an absorption-related origin (e.g. [Leighly et al. 2007](#); [Miniutti et al. 2012](#); [Liu et al. 2022](#)). Recent hard X-ray observations with *NuSTAR* also indicate that heavy absorption can account for the apparent X-ray weakness in some cases (e.g., [Wang et al. 2022](#)).

Alternatively, changes in the X-ray corona itself may also contribute to the observed variability. Variations in coronal geometry or radiative efficiency could suppress the X-ray emission while leaving the accretion disk largely unaffected. At present, the available data do not uniquely distinguish between complex absorption and intrinsic coronal variations. Nevertheless, the pronounced wavelength-dependent behavior — extreme X-ray variability accompanied by minimal changes in the optical and UV emission — indicates that the dominant mechanism is confined to the compact X-ray-emitting region rather than reflecting a global transformation of the accretion flow.

4.2. Short-term Variability: Evidence for Clumpy Structure

Within the prolonged low state, SDSS J0005+2007 continues to exhibit rapid variability on timescales of days to weeks, including epochs of non-detection followed by rebrightening. Such behavior indicates that the low state is not static. If obscuration dominates, the absorber is unlikely to be homogeneous. The rapid variability instead suggests compact structures moving across the line of sight. A natural interpretation is that the absorbing medium is clumpy, consisting of dense, compact clouds embedded within a more diffuse, partially covering wind. Occasional non-detections can then be explained by individual optically thick clumps transiting the line of sight to the compact X-ray emitting region.

Similar rapid X-ray dimming events have been reported in other quasars. For example, Liu et al. (2022) observed a radio-quiet type 1 quasar at $z \sim 2.6$ whose X-ray flux decreased by a factor of ~ 7.6 within two rest-frame days, which was interpreted as a fast-moving absorber crossing and fully covering the X-ray emitting corona. Such events support the possibility of compact absorbing structures in quasar winds.

The duration of obscuration events can be used to estimate the physical size of the transiting clumps. The crossing time, t_{cross} , for an absorber of projected size r_{abs} moving with Keplerian velocity at an orbital radius r_{orb} is given by

$$t_{\text{cross}} \approx 0.7 \left(\frac{r_{\text{orb}}}{\text{light-day}} \right)^{3/2} M_6^{-1/2} \arcsin \left(\frac{r_{\text{abs}}}{r_{\text{orb}}} \right) \text{ yr}, \quad (1)$$

where r_{orb} is the orbital radius of the absorber, M_6 is the black hole mass in units of $10^6 M_\odot$, and r_{abs} is the projected size of the absorber.

To test this scenario, we assume the absorber is located at a distance comparable to the UV/optical emitting region, $r_{\text{orb}} \approx 40\text{--}70$ light-days, as suggested by the blackbody fits. Assuming a clump size an order of magnitude smaller than the orbital radius ($r_{\text{abs}} \approx 0.1 r_{\text{orb}}$), and adopting the estimated black hole mass, we obtain a crossing time of $\sim 180\text{--}220$ days. This timescale is broadly consistent with the duration of the possible non-detection interval, providing tentative support for a compact cloud orbiting within a larger-scale wind structure.

In the clumpy-absorber scenario, the assumed absorber distance is comparable to the expected broad-line region (BLR) size estimated from the empirical $R_{\text{BLR}}\text{--}L_{5100}$ relation. Optically thick clumps transiting across our line of sight could therefore in principle also influence the ionizing continuum incident on the BLR. In practice, the optical continuum and broad emission-line profiles remain remarkably stable over decade-long timescales, indicating that the BLR is not significantly affected during the X-ray low states. Furthermore, we estimate the Balmer decrement and obtain a value of ~ 3 , comparable to the intrinsic broad-line ratio expected for unobscured type 1 AGNs ($f_{\text{H}\alpha}/f_{\text{H}\beta} \approx 3$; Veilleux & Osterbrock 1987; Dong et al. 2008), suggesting that the BLR is not strongly affected by dust obscuration. Together, these results suggest that the absorbing material either subtends only a limited covering fraction as viewed from the BLR or is largely confined to our direct line of sight toward the compact X-ray-emitting region.

Nevertheless, some aspects of the observed variability remain difficult to reconcile with a simple clumpy-absorber scenario. In particular, the rapid flux

rise observed in September 2021 occurs on a much shorter timescale (~ 12 days), which would require sharp column-density gradients or highly structured absorbing material at the cloud boundary. Such rapid variability may instead indicate that intrinsic changes in the X-ray corona also contribute to the observed behavior. Rapid variations in coronal geometry and energetics on timescales of days have been proposed to explain extreme X-ray variability in AGNs (e.g., Ricci et al. 2020; Wu et al. 2020; Papoutsis et al. 2026; Xu et al. 2025). Several physical scenarios involving variable coronae have been suggested, including “failed jet” configurations and extreme reprocessing models (e.g., Ghisellini et al. 2004; Lawrence 2018). Therefore, although a clumpy absorber crossing our line of sight provides a natural explanation for the long-term X-ray suppression, intrinsic coronal variability cannot currently be ruled out. Future broadband X-ray monitoring with improved spectral sensitivity will be important for distinguishing between variable absorption and intrinsic coronal variability in SDSS J0005+2007.

4.3. Comparison with X-ray-Weak Quasars

X-ray-weak quasars constitute a population of AGNs whose X-ray emission is significantly weaker than expected from their UV luminosities. These objects typically lie below the canonical $\alpha_{\text{ox}}\text{--}L_{2500\text{\AA}}$ relation defined for normal radio-quiet quasars (Steffen et al. 2006), often corresponding to X-ray weakness factors of $f_{\text{weak}} \gtrsim 10$. As shown by the spectral energy distribution analysis presented in Section 3.4, SDSS J0005+2007 undergoes a clear transition into an X-ray-weak state.

Figure 7 places SDSS J0005+2007 in the context of several well-studied X-ray-weak quasars, including PHL 1811 and its analogs. During the high-flux states, SDSS J0005+2007 lies close to the locus of typical quasars, with α_{ox} values consistent with the expected relation, indicating a normal disk-corona configuration. However, during the low-flux epochs the source moves substantially below the relation, entering the region populated by known X-ray-weak quasars such as PHL 1811 (Leighly et al. 2007) and PHL 1092 (Miniutti et al. 2012). The inferred $\Delta\alpha_{\text{ox}}$ values and X-ray weakness factors are comparable to those observed in these systems, demonstrating that SDSS J0005+2007 reaches a level of X-ray weakness typical of this extreme population. This behavior suggests that at least a fraction of X-ray-weak quasars may represent transient episodes of X-ray suppression rather than intrinsically distinct objects.

Similar transitions have been observed in several quasars. As prominent examples, SDSS J0751+2914

(Liu et al. 2019), SDSS J0814+5325 (Huang et al. 2023), SDSS J1350+2618 (Liu et al. 2022), and SDSS J1539+3954 (Ni et al. 2020) all exhibit dramatic X-ray variability with little corresponding UV change. In particular, SDSS J1539+3954 shows an X-ray flux increase by a factor of $\gtrsim 20$ while its UV continuum remained constant, interpreted as the transverse motion of a geometrically thick inner disk. More recently, Wang et al. (2024) reported a factor of ~ 32 variation in the ultraluminous quasar SDSS J1521+5202 over 17 yr, supporting models in which variable absorption regulates the observed X-ray emission. In addition, Zhang et al. (2023) reported two X-ray-weak quasars that returned to normal X-ray brightness, further indicating that X-ray-weak phases can be transient.

SDSS J0005+2007 also shares several properties with other X-ray-weak AGNs. The relatively weak Mg II emission and moderately high Eddington ratio place it in a parameter space overlapping with WLQs, many of which are X-ray weak. Moreover, the extreme variability is confined primarily to the X-ray band, while the UV and optical emission remain largely stable, a behavior commonly observed in X-ray-weak quasars (Miniutti et al. 2012; Ni et al. 2020; Zhang et al. 2023; Huang et al. 2023).

The source also shows similarities to the NLS1 galaxy RX J0134.2–4258, which exhibits strong X-ray variability together with weak high-ionization emission lines (Jin et al. 2023). In addition, SDSS J0005+2007 resembles the prototypical X-ray-weak NLS1 PHL 1092 (Miniutti et al. 2012), which shows dramatic X-ray dimming without significant UV variability and stable optical spectra. These similarities suggest that a subset of NLS1s may experience episodes of extreme X-ray weakness, possibly related to complex and variable inner disk–corona structures.

4.4. *Could be a Tidal Disruption Event?*

The majority of X-ray-selected tidal disruption events (TDEs) demonstrate X-ray decay over a timescale spanning months to a year, a phenomenon attributed to the decline in accretion rates (Saxton et al. 2020). While extremely rare, some TDEs exhibit X-ray emissions lasting up to a decade, with the notable exception of XJ1500+015 (Lin et al. 2017). In contrast to typical TDE behavior, SDSS J0005+2007 displays persistent X-ray emissions for over 20 years, followed by a sharp decline over several years.

The emission line profiles in TDEs are known to evolve over time, with broad TDE lines typically narrowing as time progresses (Holoien et al. 2016). This change is attributed to the decreasing optical depth for electron

scattering in the line emission region (Roth et al. 2018). However, the emission lines of SDSS J0005+2007 remain largely unchanged throughout the entire event.

Therefore, given the aforementioned considerations, the TDE scenario for SDSS J0005+2007 appears less likely.

5. SUMMARY

We present a comprehensive multi-epoch study of SDSS J0005+2007, a quasar that transitions from an X-ray-normal state to an X-ray-weak state. Over a timescale of ~ 5 yr, the 0.2–10 keV X-ray flux declines by more than an order of magnitude, reaching weakness factors of $f_{\text{weak}} \gtrsim 10$ –100 in the faintest epochs. During the high states, the X-ray spectrum is persistently soft, whereas the stacked low-state spectrum shows substantial flux suppression together with indications of spectral hardening.

In contrast, the UV continuum varies only mildly (~ 0.3 mag), and the optical continuum, broad emission lines, and mid-infrared emission remain stable over decade-long timescales. The source moves from the canonical $\alpha_{\text{ox}}-L_{2500\text{\AA}}$ relation into the X-ray-weak regime during the low states, while retaining the optical spectroscopic characteristics of a normal type 1 quasar.

The pronounced wavelength dependence of the variability provides strong physical constraints. The stability of the optical continuum and broad-line region indicates that the accretion disk structure and photoionizing luminosity remain largely intact, whereas the dramatic suppression of the X-ray emission must originate in the compact coronal region or along our line of sight to it. The spectral hardening observed in the low state, together with the viability of ionized partial-covering models, is consistent with an absorption-driven scenario in which variable, largely dust-free gas located interior to or comparable to the broad-line region modulates the observed X-ray emission. Such behavior is similar to that observed in several X-ray-weak quasars and is consistent with clumpy inner disk winds or shielding-gas configurations.

While intrinsic coronal variations cannot be excluded, the multi-wavelength constraints disfavor a global accretion-state transition. Given the specific observed characteristics, the possibility of a TDE scenario for SDSS J0005+2007 is low. SDSS J0005+2007 therefore provides further evidence that extreme X-ray weakness can arise as a transient phase in otherwise normal quasars. Continued monitoring will be essential to constrain the geometry and location of the absorbing material and to determine the recurrence timescale of the X-ray-weak phase.

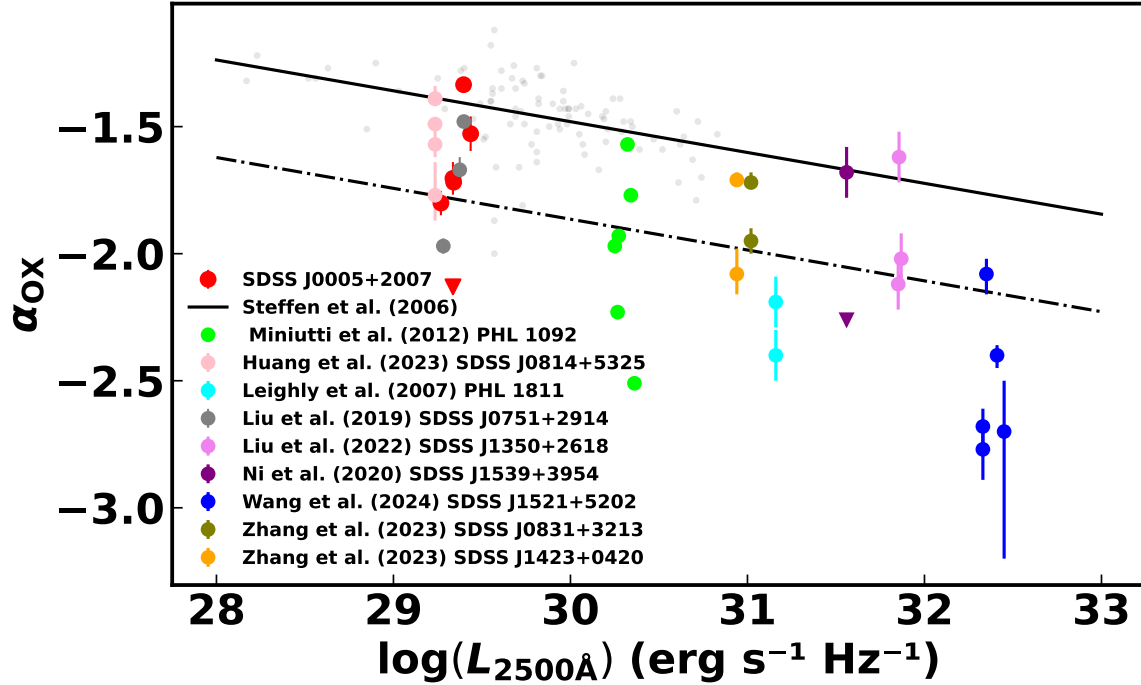


Figure 7. X-ray-to-optical slope (α_{OX}) versus the monochromatic luminosity at rest-frame 2500 Å. The red points show SDSS J0005+2007 at different epochs. Gray points represent typical AGNs from Steffen et al. (2006), and the solid black line shows their best-fit $\alpha_{\text{OX}}-L_{2500\text{Å}}$ relation. Large colored symbols denote individual X-ray weak quasars with multi-epoch observations, illustrating their variability trajectories. These include PHL 1092 (Miniutti et al. 2012), the prototype PHL 1811 (Leighly et al. 2007), SDSS J0751+2914 (Liu et al. 2019), SDSS J0814+5325 (Huang et al. 2023), SDSS J1350+2618 (Liu et al. 2022), SDSS J1539+3954 (Ni et al. 2020), SDSS J1521+5202 (Wang et al. 2024), and the variable WLQs (SDSS J0831+3213 and SDSS J1423+0420) reported by Zhang et al. (2023). The dot-dashed line marks an X-ray weakness factor of $f_{\text{weak}} = 10$ ($\Delta\alpha_{\text{OX}} = -0.384$).

ACKNOWLEDGMENTS

We acknowledge the supports from National Natural Science Foundation of China (NSFC; grant Nos.12573110, 12133001), the Shenzhen Science and Technology Program (JCYJ20230807113910021) and the Natural Science Foundation of Top Talent of SZTU(GDRC202208).

Spectroscopic observations were obtained with the Palomar 200-inch Hale Telescope at Palomar Observatory using the Next Generation Palomar Spectrograph

(NGPS). We thank the Palomar Observatory staff for their support during the observations. This work makes use of observational data obtained with Einstein Probe, a space mission supported by Strategic Priority Program on Space Science of Chinese Academy of Sciences, in collaboration with ESA, MPE and CNES (Grant No. XDA15310000), the Strategic Priority Research Program of the Chinese Academy of Sciences (Grant No. XDB0550200), and the National Key R&D Program of China (2022YFF0711500).

REFERENCES

- Ai, Y. L., Yuan, W., Zhou, H. Y., Wang, T. G., & Zhang, S. H. 2011, *ApJ*, 727, 31
- Ai, Y., Dou, L., Yang, C., et al. 2020, *ApJL*, 890, L29
- Arnaud, K. A. 1996, *Astronomical Data Analysis Software and Systems V*, 101, 17
- Boller, T., Liu, T., Weber, P., et al. 2021, *A&A*, 647, A6
- Cheng, X., Wu, J., & Wu, Q. 2025, *ApJ*, 994, 213
- Chira, M., Georgakakis, A., Ruiz, A., et al. 2026, *MNRAS*, 545, 1, staf1905. doi:10.1093/mnras/staf1905
- Dalla Bontà, E., Peterson, B. M., Bentz, M. C., et al. 2020, *ApJ*, 903, 112
- Du, P. & Wang, J.-M. 2019, *ApJ*, 886, 1, 42
- Diamond-Stanic, A. M., Fan, X., Brandt, W. N., et al. 2009, *ApJ*, 699, 782

- Dong, X., Wang, T., Wang, J., et al. 2008, *MNRAS*, 383, 2, 581
- Drake, A. J., Djorgovski, S. G., Mahabal, A., et al. 2013, *ApJ*, 763, 32
- Evans, P. A., Page, K. L., Osborne, J. P., et al. 2020, *ApJS*, 247, 54
- Fan, X., Strauss, M. A., Gunn, J. E., et al. 1999, *ApJL*, 526, L57
- Magnier, E. A., Schlafly, E. F., Finkbeiner, D. P., et al. 2020, *ApJS*, 251, 1, 6
- Gaia Collaboration, Vallenari, A., Brown, A. G. A., et al. 2023, *A&A*, 674, A1
- Greene, J. E. & Ho, L. C. 2005, *ApJ*, 630, 1, 122
- Gibson, R. R., Brandt, W. N., & Schneider, D. P. 2008, *ApJ*, 685, 773
- Gibson, R. R., & Brandt, W. 2012, *ApJ*, 746, 54
- Giustini, M. & Proga, D. 2019, *A&A*, 630, A94
- Ghisellini, G., Haardt, F., & Matt, G. 2004, *A&A*, 413, 535
- Grupe, D., Komossa, S., & Saxton, R. 2015, *ApJL*, 803, L28
- Guo, H., Shen, Y., & Wang, S. 2018, *Astrophysics Source Code Library*. ascl:1809.008
- Ha, T., Dix, C., Matthews, B. M., et al. 2023, *ApJ*, 950, 2, 97
- Holoien, T. W. S., Kochanek, C. S., Prieto, J. L., et al. 2016, *MNRAS*, 455, 2918
- Huang, J., Luo, B., Brandt, W. N., et al. 2023, *ApJ*, 950, 18
- Huang, J., Luo, B., Brandt, W. N., et al. 2026, [arXiv:2605.22918](https://arxiv.org/abs/2605.22918). doi:10.48550/arXiv.2605.22918
- Jana, A., Kumari, N., Nandi, P., et al. 2021, *MNRAS*, 507, 687
- Jansen, F., Lumb, D., Altieri, B., et al. 2001, *A&A*, 365, L1
- Jiang, H., Hu, Z., Xu, M., et al. 2018, *Proc. SPIE*, 10702, 107022L
- Jiang, Y.-F., Blaes, O., Stone, J. M., & Davis, S. W. 2019, *ApJ*, 885, 144
- Jin, C., Done, C., Ward, M., et al. 2023, *MNRAS*, 518, 6065
- Kalberla, P. M. W., Burton, W. B., Hartmann, D., et al. 2005, *A&A*, 440, 775
- Krawczyk, C. M., Richards, G. T., Mehta, S. S., et al. 2013, *ApJS*, 206, 4
- Krumpe, M., Husemann, B., Tremblay, G., et al. 2017, *A&A*, 607, L9
- Laurenti, M., Piconcelli, E., Zappacosta, L., et al. 2022, *A&A*, 657, A57
- Lawrence, A. 2018, *Nature Astronomy*, 2, 102
- Leighly, K. M., Halpern, J. P., Jenkins, E. B., & Casebeer, D. 2007, *ApJS*, 173, 1
- Lin, D., Guillochon, J., Komossa, S., et al. 2017, *Nature Astronomy*, 1, 0033. doi:10.1038/s41550-016-0033
- Liu, H., Luo, B., Brandt, W. N., et al. 2019, *ApJ*, 878, 79
- Liu, Z., Liu, H.-Y., Cheng, H., Qiao, E., & Yuan, W. 2020, *MNRAS*, 492, 2335
- Liu, H., Luo, B., Brandt, W. N., et al. 2022, *ApJ*, 930, 53
- Luo, B., Brandt, W. N., Hall, P. B., et al. 2015, *ApJ*, 805, 122
- Lusso, E., & Risaliti, G. 2016, *ApJ*, 819, 154
- Mainzer, A., Bauer, J., Grav, T., et al. 2011, *ApJ*, 731, 1, 53
- Masci, F. J., Laher, R. R., Rusholme, B., et al. 2019, *PASP*, 131, 018003
- Mehdipour, M., Kriss, G., Kaastra, J., et al. 2021, *A&A*, 652, A150
- Middei, R., Vagnetti, F., Bianchi, S., et al. 2017, *A&A*, 599, A82
- Miniutti, G., Brandt, W. N., Schneider, D. P., et al. 2012, *MNRAS*, 425, 1718
- Morrissey, P., Schiminovich, D., Barlow, T. A., et al. 2005, *ApJL*, 619, L7
- Nardini, E., Lusso, E., Risaliti, G., et al. 2019, *A&A*, 632, A109
- Ni, Q., Brandt, W. N., Luo, B., et al. 2018, *MNRAS*, 480, 5184
- Ni, Q., Brandt, W. N., Luo, B., et al. 2020, *ApJL*, 889, L37
- Ni Q., Brandt W. N., Luo B., et al. 2022, *MNRAS*, 511, 5251
- Oke, J. B., & Gunn, J. E., 1982, *PASP*, 94, 586
- Poole, T. S., et al. 2008, *MNRAS*, 383, 627
- Paliya, V. S., Stalin, C., Domínguez, A., & Saikia, D. 2024, *MNRAS*, 527, 7055
- Papoutsis, M., Papadakis, I. E., Panagiotou, C., et al. 2026, *A&A*, 705, A257
- Parker, M. L., Alston, W. N., Härer, L., et al. 2021, *MNRAS*, 508, 1798
- Plotkin, R. M., Anderson, S. F., Brandt, W. N., et al. 2010b, *AJ*, 139, 390
- Prochaska, J., Hennawi, J., Westfall, K., et al. 2020, *The Journal of Open Source Software*, 5, 56, 2308. doi:10.21105/joss.02308
- Pu X., Luo B., Brandt W. N., et al. 2020, *ApJ*, 900, 141
- Rakshit, S., Stalin, C. S., & Kotilainen, J. 2020, *ApJS*, 249, 1, 17
- Reeves, J., Done, C., Pounds, K., et al. 2008, *MNRAS*, 385, L108
- Reeves, J., & Braitto, V. 2019, *ApJ*, 884, 80
- Reich, M., Brandt, W. N., Luo, B., et al. 2026, [arXiv:2603.24673](https://arxiv.org/abs/2603.24673). doi:10.48550/arXiv.2603.24673
- Ricci, C., Kara, E., Loewenstein, M., et al. 2020, *ApJL*, 898, 1, L1
- Roming, P. W. A., Kennedy, T. E., Mason, K. O., et al. 2005, *SSRv*, 120, 95
- Roth, N., & Kasen, D. 2018, *ApJ*, 855, 54

- Saxton, R., Komossa, S., Auchettl, K., & Jonker, P. G. 2020, *SSRv*, 216, 85
- Schlafly, E. F., & Finkbeiner, D. P. 2011, *ApJ*, 737, 103
- Shen, Y., Grier, C. J., Horne, K., et al. 2024, *ApJS*, 272, 26
- Steffen, A. T., Strateva, I., Brandt, W. N., et al. 2006, *AJ*, 131, 2826
- Sunyaev, R., & Titarchuk, L. 1980, *A&A*, 86, 121
- Tananbaum, H., Avni, Y., Branduardi, G., et al. 1979, *ApJL*, 234, L9
- Timlin, J. D., III, Brandt, W. N., Zhu, S., et al. 2020, *MNRAS*, 498, 4033
- Veilleux, S. & Osterbrock, D. E. 1987, *ApJS*, 63, 295
- Voges, W., Aschenbach, B., Boller, T., et al. 2000, *IAUC*, 7432, 3
- Wang, J.-M., Qiu, J., Du, P., & Ho, L. C. 2014, *ApJ*, 797, 65
- Wang, Y., Kaastra, J., Mehdipour, M., et al. 2022, *A&A*, 657, A77
- Wang S., Brandt W. N., Luo B., et al. 2024, [arXiv:2408.16060](https://arxiv.org/abs/2408.16060)
- Wang, H., Ai, Y., Zhang, Y., et al. 2025, *ApJ*, 985, 23
- WISE Team 2020, NEOWISE 2020 Data Release, IPAC, [doi:10.26131/IRSA144](https://doi.org/10.26131/IRSA144)
- Wu, J., Brandt, W. N., Hall, P. B., et al. 2011, *ApJ*, 736, 28
- Wu, J., Brandt, W. N., Hall, Anderson, Scott F., et al. 2012, *ApJ*, 747, 10
- Wu, Y.-J., Wang, J.-X., Cai, Z.-Y., et al. 2020, *Science China Physics, Mechanics, and Astronomy*, 63, 12, 129512
- Xu, X., Ding, N., & Gu, Q. 2025, *MNRAS*, 543, 4, 3981
- Yang, Q., Wu, X.-B., Fan, X., et al. 2018, *ApJ*, 862, 109
- Yang, J., Fan, X., Wang, F., et al. 2022, *ApJL*, 924, L25
- Yang, Q., Green, P. J., MacLeod, C. L., et al. 2023, *ApJ*, 953, 61
- Yang, H., & Yuan, F. 2024, [arXiv:2408.16595](https://arxiv.org/abs/2408.16595)
- Yuan, F., & Narayan, R. 2014, *ARA&A*, 52, 529
- Yuan, W., Zhang, C., Chen, Y., et al. 2022, *Handbook of X-ray and Gamma-ray Astrophysics*, 86. [doi:10.1007/978-981-16-4544-0_151-1](https://doi.org/10.1007/978-981-16-4544-0_151-1)
- Zhang Z., Luo B., Brandt W. N., et al. 2023, *ApJ*, 954, 159